

Effect of directionality of AZ31 magnesium alloy sheets produced by continuous variable cross-section direct extrusion on corrosion behavior

Cheng Guo Ma*, Wen Kang**

School of Materials Science and Chemical Engineering, Harbin University of Science and Technology, Harbin 150040, P. R. China

Received 1 May 2021, received in revised form 14 October 2021, accepted 15 October 2021

Abstract

The orientation effect of AZ31 alloy sheets prepared by continuous variable cross-section direct extrusion (CVCDE) on corrosion properties was studied by electrochemical methods. The results show that after CVCDE, the uniformity of magnesium alloy sheet in different directions is different, the grains in the extrusion direction (ED) are more fine and uniform, and the crystal planes in the sheet plane perpendicular to different directions are different. Due to the deflection of the basal and pyramidal plane towards the compression direction, the main crystal planes in the plane perpendicular to transverse direction (TD) are (0002), while the crystal planes perpendicular to ED are (10 $\bar{1}$ 0) and (11 $\bar{2}$ 0). In electrochemical impedance spectroscopy, the curve can be divided into two stages with time: the gradual formation of the corrosion film and the thickness of the corrosion layer. The thickness of the corrosion layer is an important factor causing the difference of corrosion properties in different directions. Corrosion in different directions begins with filiform corrosion and gradually develops into crevice corrosion and pitting. The (0002) crystal plane perpendicular to TD is easier to form pitting corrosion than the (10 $\bar{1}$ 0) and (11 $\bar{2}$ 0) crystal planes perpendicular to ED.

Key words: AZ31 magnesium alloy, sheet, electrochemistry, continuous variable cross-section direct extrusion (CVCDE), corrosion resistance

1. Introduction

Magnesium and its alloys have plentiful resources, excellent comprehensive properties, and broad prospects [1–3]. Magnesium alloys are the lowest density metals used in structural applications, and this feature is attractive for energy-saving and weight loss in the mechanical industry [4–6]. However, the poor corrosion resistance seriously restricts further wide-ranging and deep-level application of magnesium and its alloys. The equilibrium potential of magnesium is negative in metals, -2.74 (V), which is chemically active and is susceptible to chemical and electrochemical corrosion [7–9]. The PBR (Pilling-Bedworth Ratio) value of MgO formed on the surface of the magnesium is only 0.73 (< 1) [10], and the surface film is porous and easily broken. Therefore, the protection capacity

of the magnesium matrix is poor in the atmosphere, ocean, and other environments, which is not conducive to a wide range of applications. This is a substantial obstacle to using magnesium alloys in key applications in the automotive and aerospace industries. The components may be affected by high mechanical load and corrosive environment, resulting in severe damage to their performance and rapid decline in service life [11–13].

To improve the corrosion resistance of magnesium alloys, people were committed to revealing the relationship between microstructure and corrosion properties [14, 15]. On the one hand, the grain size affects the corrosion behavior. According to Zou et al. [16], fine and uniform dynamic recrystallized grains can improve the corrosion resistance of Mg-4Zn alloy sheets. At the same time, it is believed that grain

*Corresponding author: tel: 13796004102; e-mail address: 88528367@163.com

**Corresponding author: e-mail address: lukaskangwen@163.com

boundaries can be used as corrosion barriers to resist the occurrence of corrosion. In the study of Yang et al. [17], magnesium alloy sheets with many twins ($\sim 52\%$) have good corrosion resistance, mainly because more grain boundaries introduced by tensile twins make the microstructure of the alloy more uniform thus inhibiting the occurrence of corrosion behavior. On the other hand, the texture characteristics of crystals also affect corrosion behavior. He et al. [18] studied the mechanical properties and corrosion resistance of magnesium alloy sheets in terms of texture symmetry. The results showed that the introduction of symmetrical weak basal texture could significantly improve the sheet isotropy of magnesium alloy, improve its comprehensive mechanical properties, and effectively improve the corrosion resistance of magnesium alloy sheets. Song et al. [19] and Luo et al. [20] reported that the surface composed of (0001) basal plane was more corrosion resistant and electrochemically stable than the surface composed of (10–10) and (11–20) crystal planes. The preliminary results show that the corrosion resistance of AZ31 alloy can be improved by adjusting the microstructure and texture of magnesium alloy.

Grain refinement, second phase refinement, second phase rearrangement, dislocation formation, and twin formation can be made through the comprehensive action of deformation and temperature in the hot extrusion process, which provided a possible way to improve the corrosion and mechanical properties of magnesium alloy [21]. Haroush et al. [22] found that AZ80 magnesium alloy extruded at a relatively low temperature of 250 °C showed the best corrosion resistance due to the minimum dislocation density and grain size. Zhang et al. [23] systematically studied the effects of different surface textures on the corrosion behavior of extruded Mg-4Al-1Sn-1Zn alloy sheets. The results showed that the corrosion morphology and corrosion resistance of different surfaces were obviously different. The corrosion morphology was mainly determined by the distribution of the second phase and fine grain region, and the corrosion rate was more closely related to the overall texture.

In summary, magnesium alloys are a priority in responding to the “lightweight” trend, and the research on their forming and corrosion properties has also made some progress. The continuous variable cross-section direct extrusion (CVCDE) is a novel processing and forming method that integrates fine-grain preparation into the extrusion process [24]. Due to the particularity of the extrusion method, the distribution of the grain size in different directions of the extruded sheet is also different, which results in different corrosion properties along with different directions of the extruded sheet. Therefore, the corrosion resistance of magnesium alloy sheets in different directions was studied by the electrochemical method.

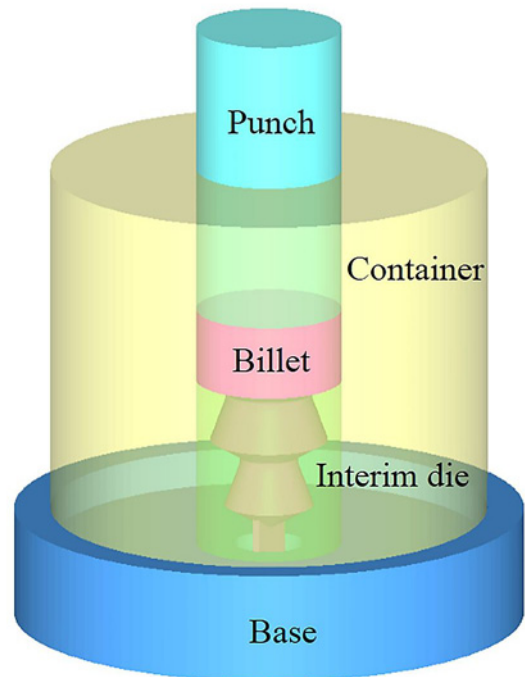


Fig. 1. The mold structure schematic of CVCDE.

2. Experimental

CVCDE is a new type of extrusion process, which cleverly adds a certain number of interim dies inside the cavity to change the overall core mold structure so that the billet can be continuously sheared in the extrusion process. And then, a larger amount of strain can be accumulated so that the grains of the extrusion parts can be refined and the mechanical properties can be improved. In the present research, the two-stage interim die and extrusion core die are used to form the die cavity, and the magnesium alloy sheet is directly extruded with CVCDE. The die structure of the CVCDE process is shown in Fig. 1.

AZ31 magnesium alloy billet was placed in the die for homogenization treatment at 350 °C. Magnesium alloy sheets with a size of 14 mm wide and thickness of 2 mm were extruded directly by CVCDE at 350 °C. The initial billet had a diameter of 40 mm, and the extrusion ratio was 44.88. Immediately after the extrusion process, it was quenched into water. The magnesium alloy sheet product after extrusion and the samples are shown in Fig. 2. The sheet-shaped specimens were embedded in an epoxy-based resin so that only the prepared surfaces were subjected to corrosion.

In Fig. 2, ED is the extrusion direction, TD is the transverse direction (perpendicular to extrusion direction), ND is the normal direction perpendicular to the sheet. The middle part of the sheet obtained by the CVCDE process was selected for the follow-

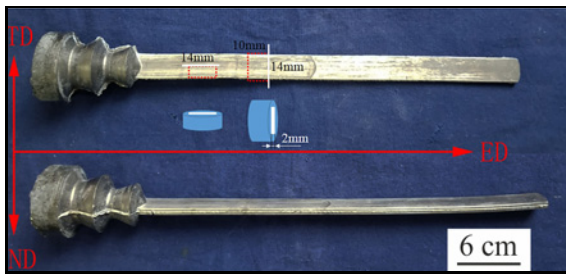


Fig. 2. Magnesium alloy sheet.

ing experimental measurement and analysis. The non-experimental surface was encapsulated with epoxy resin, and the experimental surface was polished with sandpaper to a smooth mirror surface without obvious scratches, which reduced some extra factors affecting the experimental results and ensured the validity of the measured data. The size and distribution of grain structure of magnesium alloy sheet in different directions were observed by metallographic microscope. Electrochemical experimental tests mainly included open circuit potential, Tafel curve, and electrochemical impedance spectroscopy. According to the measurement results, the difference in corrosion properties between the different directions of the extruded sheet with CVCDE was analyzed.

The electrochemical experiment used a three-electrode system in which the platinum electrode was used as an auxiliary electrode, the saturated calomel electrode was used as a reference electrode, and the magnesium alloy sheet of different orientations was used as a working electrode. Magnesium alloy sheets were cleaned by ultrasonic in alcohol after polishing to remove surface impurities, to prevent the accuracy of the experimental results from being affected. Before the electrochemical measurement, the RST5000 series electrochemical workstation was connected with wires for electrodes. The sample and electrodes were both immersed in corrosion solution (3.5% NaCl solution) for 5 min, and then the data were measured and recorded after the whole circuit system was stabilized. The magnesium alloy sheet of different directions was soaked for a different time at the same time and then ultrasonically cleaned in alcohol, dried by cold air, and preserved. The OLYMPUS-GX71-6230A metallographic microscope was used to observe microscopic morphologies of the different directions of the magnesium alloy sheet after soaking.

3. Results and discussion

3.1. Metallographic structure

Figure 3 shows metallographic photographs of

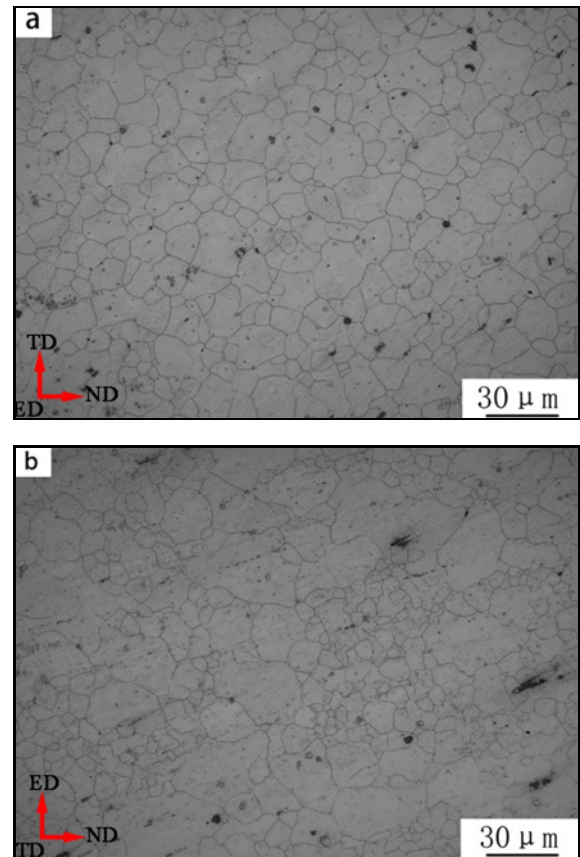


Fig. 3 Metallographic photographs of different directions: (a) ED, (b) TD.

sheets of different directions extruded by CVCDE. The average grain size in different directions is similar, but the uniformity of grain distribution is quite different.

As shown in Fig. 3a, equiaxed grains distribute uniformly in the ED, and some second-phases intermetallic Mg₁₇Al₁₂ particles scatter on grain boundaries, which indicates that dynamic recrystallization occurs during extrusion [24, 25]. Continuous shear stress refined the grains obviously, so the grain size is relatively uniform, and the grain distribution is also relatively uniform. As shown in Fig. 3b, the grain size is not uniform in the TD, and some fine equiaxed grains are wrapped in several larger grains. It is due to the fact the magnesium alloy is deformed more strongly in parallel with the extrusion direction. With the increase of deformation degree, the stored energy accumulates continuously, and the diffusion ability of grain boundary is larger, which may lead to larger grains annexing smaller grains, resulting in larger grain size.

3.2. Grain orientation

Figure 4a is the XRD of extruded magnesium alloys. It is obvious that a strong texture has formed

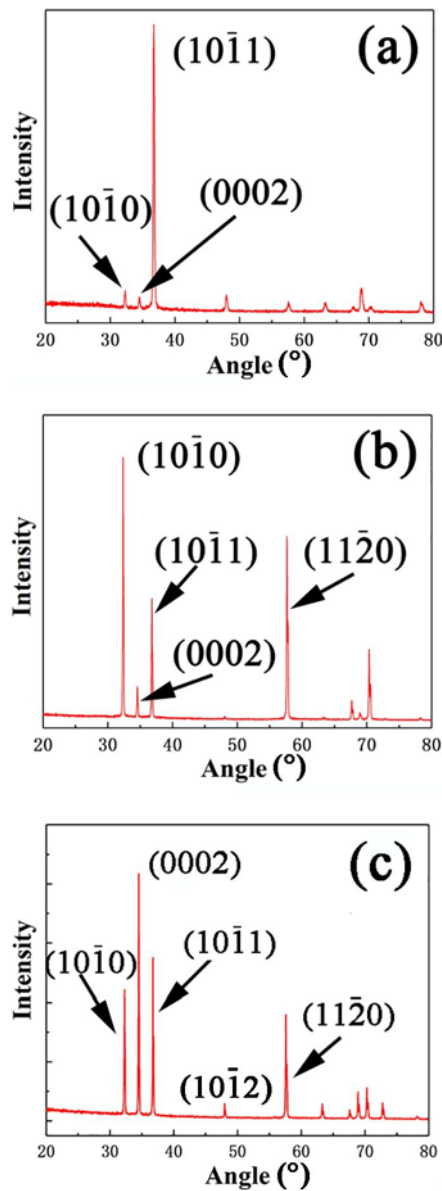


Fig. 4. XRD analysis: (a) as-cast magnesium alloys, (b) ED, (c) TD.

with high intensity at (10 $\bar{1}1$) peak because the basal planes of grains are perpendicular to the extrusion direction, forming the extrusion wire texture. After CVCDE, the grain orientation changes. In the ED of the magnesium alloy sheet, the crystal plane contained changes. The crystal planes perpendicular to the ED include (10 $\bar{1}0$), (10 $\bar{1}1$), (11 $\bar{2}0$), and a small amount of (0002) basal plane. The diffraction intensity along (10 $\bar{1}0$) increases to the peak, and the (11 $\bar{2}0$) also has a higher diffraction intensity. Therefore, the prismatic texture (10 $\bar{1}0$) and (11 $\bar{2}0$) mainly formed in the ED, as shown in Fig. 4b. From the profile in Fig. 4c, it is seen that (0002) basal planes of the majority of the grains are oriented perpendicular to TD, and the (10 $\bar{1}0$) and

(10 $\bar{1}1$) crystal planes of some grains are perpendicular to TD. The continuous variable cross-section process was applied to sheet making; when the sheet was finally formed, the billet was subjected to pressure from TD and ND, which makes the *c*-axis of the crystal deflect and form a certain texture [24]. The fundamental reason is that the activation of the basal and pyramidal slip systems causes lattice rotation. The direction normal to the basal plane rotates towards the compressive direction, and the direction normal to the pyramidal also rotates towards the compression direction. According to the critical shear stress ratio of the two slip systems, the lattice rotation caused by the basal and pyramidal slip systems may become balanced [26–28]. The compression along the ND and TD deflects the basal plane of the crystal, the crystal plane left in the ED becomes pyramidal, and the crystal plane left in the TD is mainly (0002).

The XRD results show the crystal planes contained in the macro-region of the tested sample surface. EBSD is the crystal orientation information in a micro-region, which is more accurate. From Fig. 5, we can see that the grain orientation distribution obtained by electron backscatter diffraction (EBSD) is basically consistent with Fig. 4. In the ED, the grains with the (10 $\bar{1}0$) orientation are obviously in the majority, and the distribution of grain orientation is relatively concentrated. In the TD, there are grains with three orientations, the proportion of the grains with the (0002) orientation is relatively large, and the distribution of grain orientation is relatively dispersed. (10 $\bar{1}0$) and (10 $\bar{1}1$) are also the main grain orientations in the TD. Combined with XRD results and EBSD orientation analysis, it can be seen that the grain orientation of magnesium alloy sheets in different directions is quite different, and different grain orientation distributions will have different effects on the corrosion resistance of magnesium alloy sheets.

3.3. Open circuit potential

Figure 6 shows the fluctuation of the open circuit potential of the magnesium alloy sheet of different directions extruded by CVCDE immersing for 3 h. The potential fluctuation curves of the ED and TD are included in Fig. 6.

It can be seen that there are different potential trends in two different directions. The potential of the ED stabilizes finally around -1.380 V, while that of the TD ends around -1.550 V. Thus, the open-circuit potential in the TD is more negative than that in the ED. Thermodynamically, the TD is more likely to form a tiny galvanic cell with the corrosive liquid, resulting in an anodic reaction where the anode material loses electrons to form ions. The general trend of open-circuit potential in both directions is an obvious upward trend, preserving a steady state. Volt-

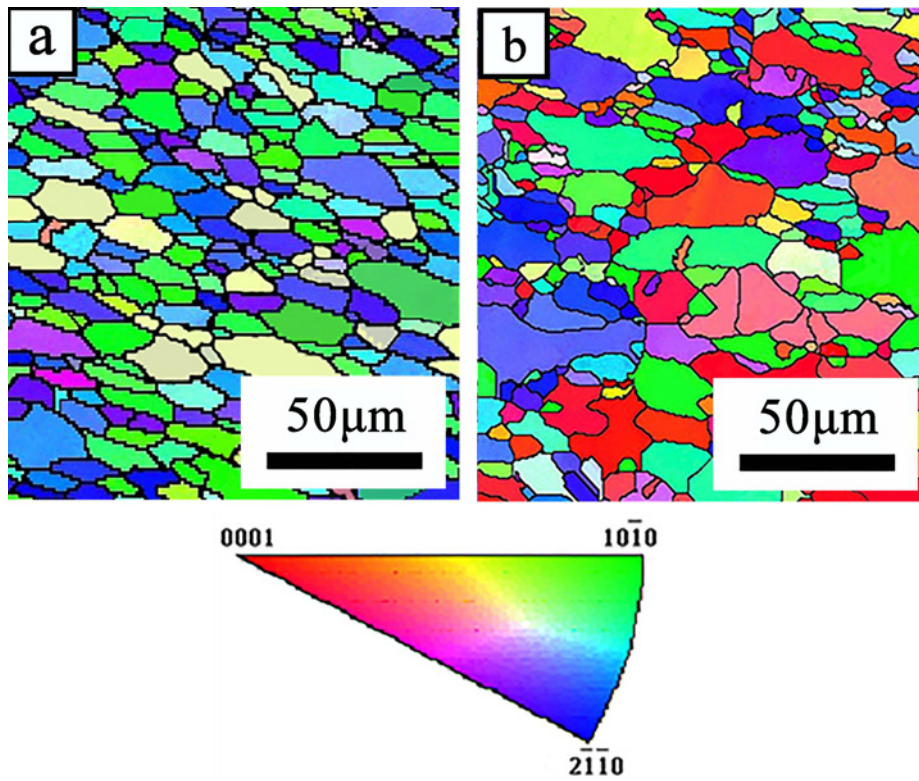


Fig. 5. Grain orientation distribution: (a) ED, (b) TD.

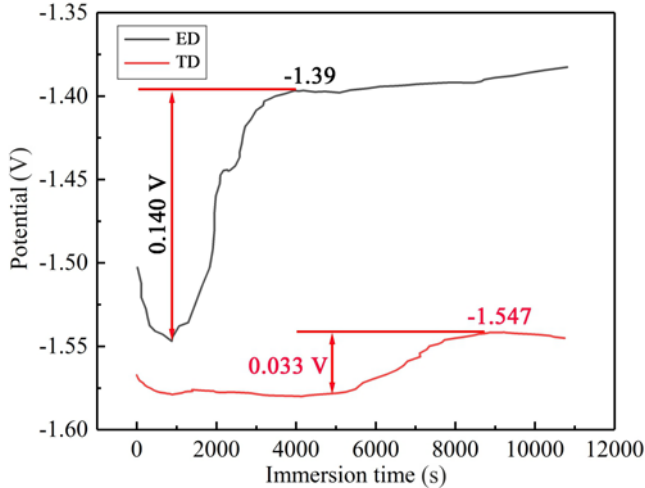


Fig. 6. Open circuit potential change of different directions.

age drop appears in both ED and TD at the initial stage of measuring open-circuit potential, mainly due to solution resistance. The potential in the ED rises rapidly, and it rises to -1.390 V at about 3500 s. From the initial stage potential to the steady-state for about 2000 s, and then the potential remains basically stable. The potential in the TD stabilizes for a period of time around -1.580 V and begins to rise gradually until 5000 s. Then, it remains stable around -1.57 V and

lasts 2000 s during the rise. In the same period, the potential of two different directions reaches a steady state, while the ED increases from -1.530 to -1.390 V, and the potential increases by 0.140 V. The TD increases from -1.580 to -1.547 V, and the potential increases by 0.033 V. It can be seen that the potential in the ED changes more rapidly. At the initial stage of immersion in corrosion solution, the corrosion tendency in the ED is greater than that in the TD.

In addition, since the open-circuit potential in the ED takes less time to reach a stable value than that in the TD, the time when the corrosion film is formed in the ED is shorter than that in the TD. When the corrosion film is completely deposited on the surface, the potential gradually becomes steady. According to the study of Hagihara et al. [29], different orientations affect the corrosion rate. The corrosion rates increased in the order $(0002) < (11\bar{2}0) < (10\bar{1}0) < (11\bar{2}3) < (10\bar{1}2)$. Therefore, the open-circuit potential in ED is stabilized faster. Due to the existence of a small part of $(10\bar{1}2)$ orientation in TD, the potential is smaller.

3.4. Polarization curve

Figure 7 shows Tafel curves in different directions of the magnesium alloy sheet extruded by CVCDE.

The different curves show the corrosion behavior difference between the two directions, which mainly depends on the setting extrusion speed, die structure,

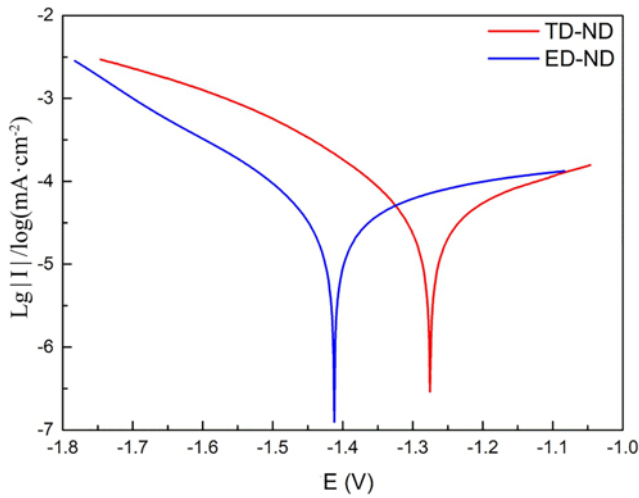


Fig. 7. Tafel curves of different directions.

and other process parameters of CVCDE. Therefore, there are differences in the grain size and orientation in different directions of the extruded magnesium alloy sheet, thereby affecting the comprehensive properties of the sheet in different directions. The grains in the ED are relatively small, and the distribution is relatively uniform, but the grain size in the TD is different. The uniformity of grain size can make the corrosion potential move towards positive potential. It can be seen the self-corrosion potential E_{corr} in the ED is between -1.4 and -1.3 V, and the self-corrosion potential E_{corr} in the TD is between -1.6 and -1.5 V, so the difference between the two is about 200 mV. The difference in self-corrosion potential is mainly due to the difference in the grain size. According to the comparison of self-corrosion potentials, the self-corrosion potential in the TD is lower, and the corrosion tendency should have been more severe in the corrosion solution because of its lower potential. However, the corrosion current densities of two different directions are similar; the current density in the ED is $3.016843\text{E-}05$ A cm^{-2} , and that in the TD is $2.276979\text{E-}05$ A cm^{-2} . It indicates that the corrosion rates achieved by the two directions are not significantly different. The reason is that although the grain size of the TD is slightly larger, the electrochemical activity of (0002) basal texture is weak [30], which makes up for its defect of larger grain size, thus weakening the corrosion tendency of TD caused by lower self-corrosion potential.

3.5. Electrochemical impedance spectroscopy

As shown in Fig. 8, the Nyquist plot of the magnesium alloy sheet immersed in the corrosion solution for different times is shown. Figure 8a is the impedance

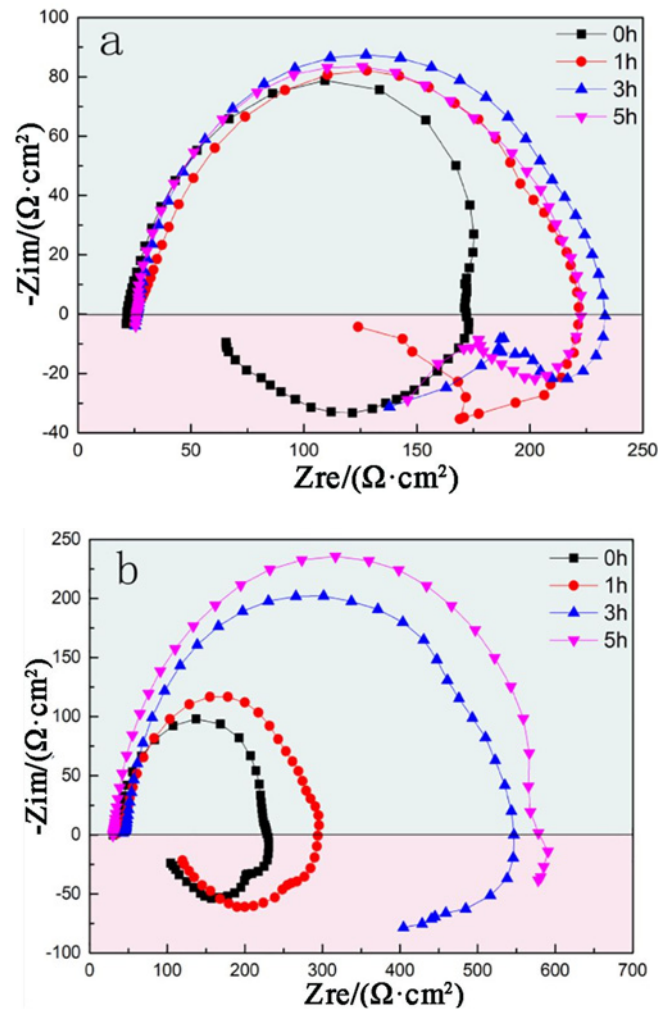


Fig. 8. Nyquist plots of different directions with time: (a) ED, (b) TD.

diagram of the ED changing with time, and Fig. 8b is the impedance diagram of the TD changing with time.

The Nyquist plot is based on the real part of the impedance as the abscissa and the negative part of the imaginary part as the ordinate. Each point in the figure represents different frequencies. The left side has high frequencies and becomes a high-frequency area, while the right side has low frequencies and becomes a low-frequency area. Huang et al. [31, 32] stressed the importance of electrochemical impedance spectroscopy (EIS) for getting quantitative information concerning the physical properties of inner barrier layers and outer porous layers. The electrochemical impedance is mainly composed of three parts, which are internal resistance $R\Omega$, electric double layer capacity Cd , and Faraday impedance Zf . Among them, $R\Omega$ is the internal resistance of the electrolyte and the electrode; electric double-layer capacity Cd is derived from the inactive ions in the electrolyte, and no

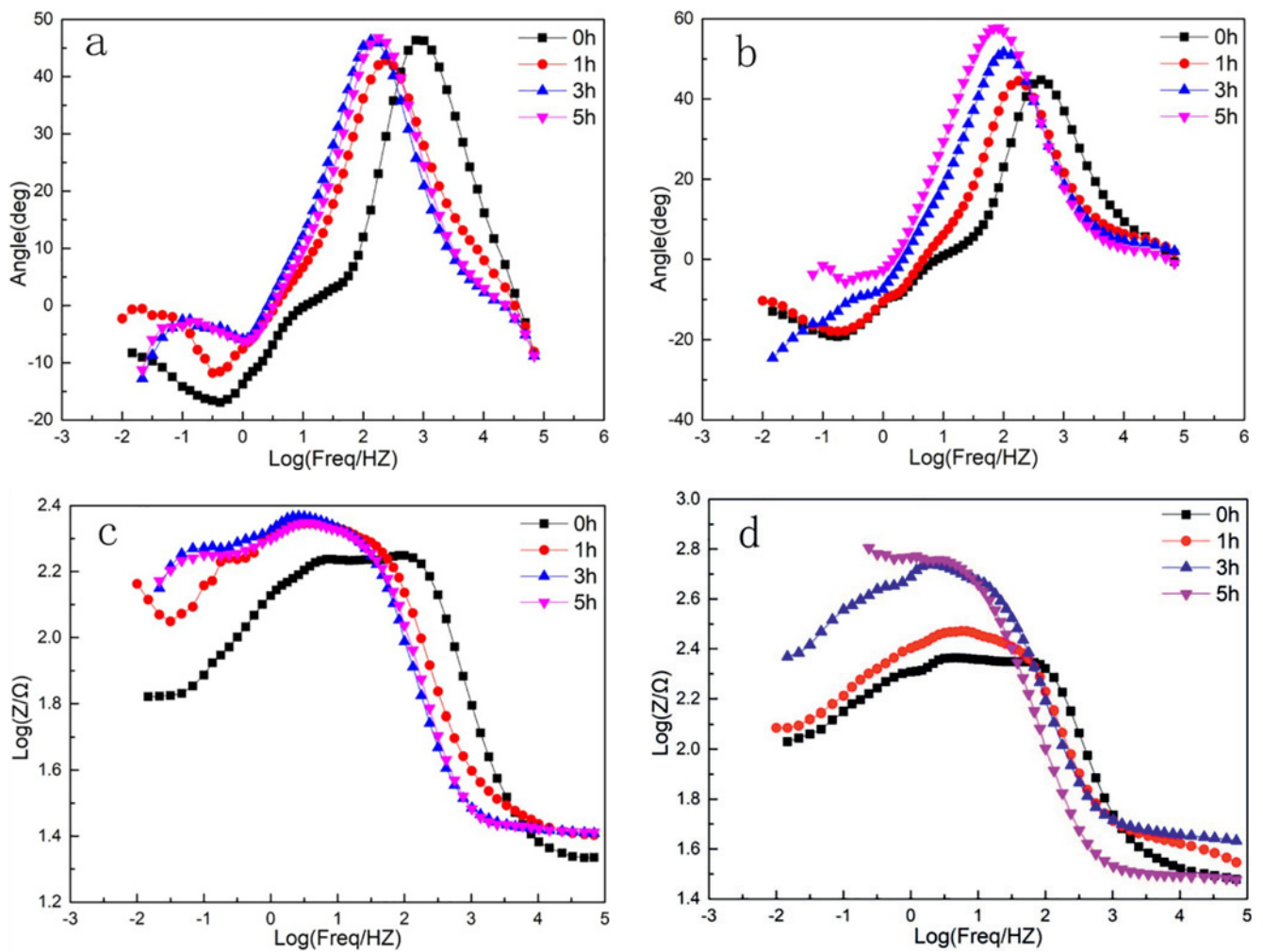


Fig. 9. Bode plots of different directions: (a) and (c) TD-ND, (b) and (d) ED-ND.

chemical reaction occurs, only changing the charge distribution; Faraday impedance Z_f is derived from the active ions in the electrolyte, which has a redox reaction and charge transfer. It can be seen that there are some similarities in the Nyquist plot of different directions. The common feature of both directions is the appearance of two capacitive loops at the medium and high frequencies. Inductive loops also appear at low frequencies, and the points in the low-frequency range are densely distributed, and the points in the high-frequency range are relatively loose. The capacitive loop in the high-frequency region is related to the properties of the oxide film. The capacitive loop is affected by the electric double layer capacity and the charge transfer resistance generated by the electrochemical corrosion of the sample in the simulated seawater. Medium frequency capacitive loops are attributed to mass transfer relaxation (probably Mg^{2+}) in the solid phase or aggregated layers. The inductive loop is generated by the parallel connection of inductance and resistance. It is due to the existence of the relaxation process of adsorbates on the electrode

surface or due to the instability of the system during the immersion. The ED changes with time, and the Nyquist plot changes are not obvious. The capacitive loops of the ED at high frequencies are overlapped. Except for the Nyquist plot measured by immersion for 0 h, the responses of the other three Nyquist plots at each frequency are basically the same. It is indicated that after immersion for 1 h, the passivation film of the ED has basically formed, and the charge transfer and the material transfer have also reached equilibrium. The TD changes with time, and the Nyquist plot changes greatly. With the prolonged immersion time in corrosion solution, the size of the high-frequency loop and medium frequency capacitive loop gradually becomes larger, especially from 1 to 3 h. It indicates that the TD occurs the electrochemical reaction continuously in the corrosion solution before immersion for 1 h. When immersed for 3 h, the Nyquist plot changes significantly, the response change of each frequency becomes smaller, and the capacitive loops of high frequency and medium frequency are similar in size. At this time, the corrosion film has covered the

entire surface of the TD. During the continuous immersion process, the main factor affecting the change of the Nyquist plot is from the gradual formation of the corrosion film to the change of the thickness of the corrosion film. Therefore, the change of the Nyquist plot with time can be divided into two stages: the gradual formation of the corrosion film and the thickening of the corrosion layer.

Comparing the Nyquist plots in the ED and TD, it can be seen that the size of the capacitive loop in the TD is always larger than the size of the capacitive loop in the ED for the same time of immersion. Especially after immersion for 3 h, the size of the capacitive loop of the two directions has a significant difference. It can be seen from Fig. 4 that after immersion for 3 h, both ED and TD are entirely covered by the corrosion film, so the reason for the large difference in the size of the capacitive loop is mainly attributed to the thickness of the corrosion layer of MgO/Mg(OH)₂. This indicates that thickness reduction resulted in reduced protection [33].

Figure 9 shows Bode plots in the different directions of magnesium alloy sheets extruded by CVCDE. The Bode plot consists of two kinds of curves: the abscissa is the logarithm of the frequency, while the ordinate is the logarithm of the impedance modulus or the phase angle of the impedance. Figures 9a,b show Bode plots of ED and TD in which the ordinate is phase angle, respectively. Figures 9c,d show Bode plots of ED and TD in which the ordinate is the logarithm of the impedance modulus, respectively. The phase angle and impedance modulus change with frequency, as can be observed in the Bode plots. It can be seen that the ED shows two-time constants, and the TD also has two-time constants. The impedance modulus in both directions also shows a general trend of increasing first and then decreasing, then approaching the level, from low frequency to high frequency. This trend is attributed to the diffusion of reactants or products in the low-frequency region and the charge transfer process in the high-frequency region. At low frequencies, the electrode process is controlled by the diffusion mass transfer step, and concentration polarization occurs. At high frequencies, the AC (alternating current) frequency is high. The anode and cathode reactions change rapidly. Therefore, the diffusion cannot occur in time, and the concentration polarization portion can be omitted. Combining the Nyquist plots and Bode plots of the two different directions after immersion for 5 h, the corresponding equivalent circuit was fitted to analyze the electrode system concretely.

If the electrode process is controlled by a charge transfer process (electrochemical reaction step) and the impedance caused by the diffusion process is negligible, the equivalent circuit of the electrochemical system can be simplified to Fig. 10. In the equivalent circuit, R_s is the solution resistance, R_{ct} is the charge

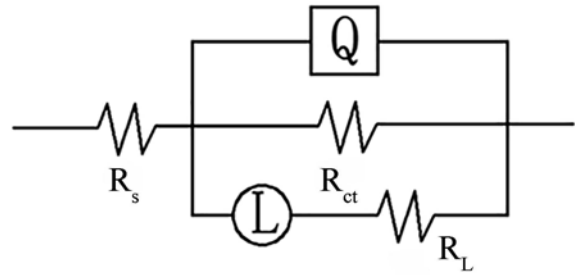


Fig. 10. Equivalent circuit.

Table 1. Fitting parameters of equivalent circuits

	R_s (ohm cm ²)	R_{ct} (ohm cm ²)	R_L (ohm cm ²)
ED	7.29	54.4	157.2
TD	8.64	155	252.3

transfer resistance, R_L is the inductive resistance, and Q is the constant phase angle element.

As shown in Fig. 10, the equivalent circuit fitted by two sections in different directions is the same. In the equivalent circuit, the equivalent inductance element L is connected in series with the inductive resistance R_L . The constant phase angle elements are often used to replace electric double layer capacities due to surface non-uniformity and dispersion effects. The fitting data obtained by simulating the impedance diagram with the above electrochemical circuit is shown in Table 1.

Table 1 shows that the solution resistance R_s , charge transfer resistance R_t , and inductive resistance R_L in the TD are significantly higher than those in the ED. The larger the R_s , the more difficult the ion exchange or Faraday process in the solution is to proceed. The larger the R_{ct} , the more complete the film on the surface of the electrode, and the more unfavorable the charge transfer. The larger the R_L , the more obvious the relaxation phenomenon caused by surface adsorption. It is indicated that the corrosion rate in the TD is significantly lower than that in the ED after 5 h of immersion.

3.6. Micromorphology

Figure 11 is the SEM of magnesium alloy sheets extruded by CVCDE after different immersion time.

As shown in Figs. 10a,b, the corrosion form in both directions is filiform corrosion which densely distributes in the form of a mesh on the corroded surface of the magnesium alloy when immersed for 1 h. With the prolonged immersion time, the corrosion degree

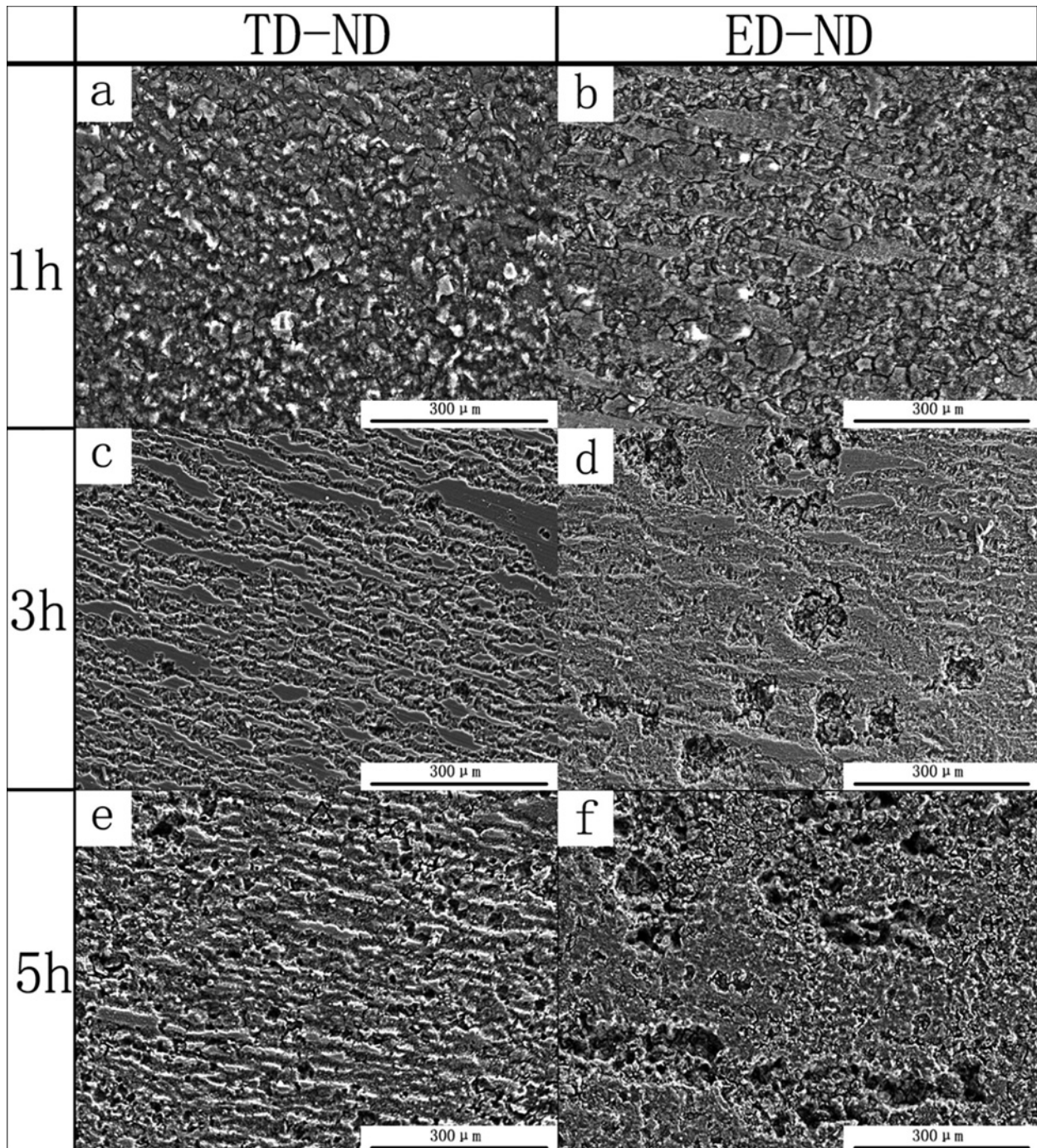


Fig. 11. (a)–(f) SEM of different directions after soaking for different times.

in both directions is gradually deepened, and filiform corrosion is used as a starting point to develop crevice corrosion and pitting corrosion. It can be seen that when immersed for 3 h, as shown in Figs. 10c,d, the ED continues to corrode mainly in the form of crevice corrosion, while the TD not only appears crevice corrosion but also pitting corrosion. The pitting corrosion is narrow and deep, and the crevice corrosion is relatively wide and shallow. It shows that the corrosion in the TD tends to proceed in the depth direction, so pit-

ting is more likely to form. When the immersion time is extended to 5 h, as shown in Figs. 10e,f, several pitting holes appear on the crevice corrosion in the ED. At this time, the entire surface had been entirely covered by the corrosion film, and it gradually began to develop in the depth direction. The pitting holes in the TD have developed into large corrosion pits. It can be seen that a number of corrosion pits are concentrated together, and meanwhile, pitting holes continue to appear and develop toward corrosion pits. In

some previous studies, the pitting morphology formed on the surface also showed crystal orientation dependence [34, 35]. Figures 3 and 4 show that in the ED, (10 $\bar{1}$ 0) is the main grain orientation, while in the TD, (0002) is the main grain orientation. According to the corrosion resistance of different orientations, although the existence of (0002) orientation in TD increases the corrosion resistance, the coarse grain and the appearance of a small part (10 $\bar{1}$ 2) lead to local pitting.

4. Conclusions

1. The grain orientation of extruded magnesium alloys is (10 $\bar{1}$ 1). After CVCDE, the grains in the ED are fine and uniform, and (10 $\bar{1}$ 0) and (11 $\bar{2}$ 0) become the main grain orientations, while the uniformity of grains in the TD is poor, and the main grain orientation is (0002). The uniformity of grain size can make the corrosion potential move towards the positive potential.

2. In the initial stage of immersion of magnesium alloy sheets prepared by CVCDE, the (10 $\bar{1}$ 1) orientation makes the open-circuit potential in ED stable faster. The existence of a small part of (10 $\bar{1}$ 2) orientations in TD results in a lower potential.

3. The characteristics of Nyquist plots of two different directions are that two capacitive loops appear at medium and high frequencies, and inductive loops also appear at the low frequency. The impedance diagram of the ED changes little with time, while that of the TD changes greatly. The change of the impedance diagram with time can be divided into two stages: the gradual formation of the corrosion film and the thickening of the corrosion layer. The thickness of the MgO/Mg(OH)₂ corrosion layer is the main factor affecting two different directions.

4. The corrosion forms in two different directions starting with filiform corrosion and gradually develops into crevice corrosion and pitting as the immersion time increases. The coarse grain and the appearance of a small part (10 $\bar{1}$ 2) lead to the occurrence of pitting corrosion.

References

- [1] J. Xiao, T. Ziming, The Influence of Properties of Vehicle-used Magnesium Alloys on the Development of Lightweight Vehicles, *New Technology & New Process* (2015).
- [2] G. Wu, C. Y. Chen, W. Ding, Current Research, Application and Future Prospect of Magnesium Alloys in Aerospace Industry, *Manned Spaceflight* (2016).
- [3] L. Mao, L. Shen, J. Chen, A promising biodegradable magnesium alloy suitable for clinical vascular stent application, *Scientific Reports* 7 (2017) 46343. [doi:10.1038/srep46343](https://doi.org/10.1038/srep46343)
- [4] M. Esmaily, J. E. Svensson, S. Fajardo, N. Birbilis, G. S. Frankel, S. Virtanen, R. Arrabal, S. Thomas, L. G. Johansson, Fundamentals and advances in magnesium alloy corrosion, *Progress in Materials Science* 89 (2017) 92–193. [doi:10.1016/j.pmatsci.2017.04.011](https://doi.org/10.1016/j.pmatsci.2017.04.011)
- [5] Y. Ogawa, D. Ando, Y. Sutou, J. Koike, A lightweight shape-memory magnesium alloy, *Science* 353 (2016) 368–370. [doi:10.1126/science.aaf6524](https://doi.org/10.1126/science.aaf6524)
- [6] Y. Liu, S. L. Cai, L. H. Dai, A new method for grain refinement in magnesium alloy, *High speed extrusion machining, Materials Science and Engineering A* 651 (2016) 878–885. [doi:10.1016/j.msea.2015.11.046](https://doi.org/10.1016/j.msea.2015.11.046)
- [7] L. T. Shi, J. Hu, X. D. Lin, L. Fang, F. Wu, J. Xie, F. M. Meng, A robust super hydrophobic PPS-PTFE/SiO₂ composite coating on AZ31 Mg alloy with excellent wear and corrosion resistance properties, *Journal of Alloys & Compounds* 721 (2017) 157–163. [doi:10.1016/j.jallcom.2017.05.333](https://doi.org/10.1016/j.jallcom.2017.05.333)
- [8] W. Yang, Z. J. Zhu, J. J. Wang, Y. C. Wu, T. Zhai, G. L. Song, Slow positron beam study of corrosion behavior of AM60B magnesium alloy in NaCl solution, *Corrosion Science* 106 (2016) 271–280. [doi:10.1016/j.corsci.2016.02.012](https://doi.org/10.1016/j.corsci.2016.02.012)
- [9] Y. Yang, F. Scenini, M. Curioni, A study on magnesium corrosion by real-time imaging and electrochemical methods: Relationship between local processes and hydrogen evolution, *Electrochimica Acta* 198 (2016) 174–184. [doi:10.1016/j.electacta.2016.03.043](https://doi.org/10.1016/j.electacta.2016.03.043)
- [10] W. Ha, J. I. Youn, Y. J. Kim, Environmentally conscious gas mixtures for magnesium melt protection, *Materials Science Forum* 510–511 (2006) 806–809. [doi:10.4028/www.scientific.net/MSF.510-511.806](https://doi.org/10.4028/www.scientific.net/MSF.510-511.806)
- [11] J. L. Zhang, C. Gu, J. Tu, Robust slippery coating with superior corrosion resistance and anti-icing performance for AZ31B Mg alloy protection, *ACS Applied Materials & Interfaces* 9 (2017) 11247–11257. [doi:10.1021/acsami.7b00972](https://doi.org/10.1021/acsami.7b00972)
- [12] M. Yang, Y. H. Liu, J. A. Liu, Y. L. Song, Effect of T6 heat treatment on corrosion resistance and mechanical properties of AM50 magnesium alloy, *Materials Research Innovations* 19 (2016) S10-259-S10-264. [doi:10.1179/1432891715Z.0000000002160](https://doi.org/10.1179/1432891715Z.0000000002160)
- [13] V. Ezhilselvi, J. Nithin, J. Balaraju, S. Subramanian, Influence of current density on the morphology and corrosion properties of MAO coatings on AZ31B magnesium alloy, *Surface & Coatings Technology* 288 (2016) 221–229. [doi:10.1016%2Fj.surfcoat.2016.01.040](https://doi.org/10.1016%2Fj.surfcoat.2016.01.040)
- [14] H. B. Yang, L. Wu, B. Jiang, W. J. Liu, H. M. Xie, J. F. Song, G. S. Huang, D. F. Zhang, F. S. Pan, Effect of microstructure on the corrosion behavior of as-cast and extruded Mg-Sn-Y alloys, *Journal of The Electrochemical Society* 167 (2020) 121503. [doi:10.1149/1945-7111/abab27](https://doi.org/10.1149/1945-7111/abab27)
- [15] R. L. Xin, M. Y. Wang, J. C. Gao, P. Liu, Q. Liu, Effect of microstructure and texture on corrosion resistance of magnesium alloy, *Materials Science Forum* 610–613 (2009) 1160–1163. [doi:10.4028/www.scientific.net/MSF.610-613.1160](https://doi.org/10.4028/www.scientific.net/MSF.610-613.1160)
- [16] Z. Zou, J. Chen, H. Yan, B. Su, X. Gong, Microstructure, bio-corrosion behavior, and corrosion residual strength of high strain rate rolled Mg-4Zn alloy sheet, *Journal of Materials Engineering & Performance* 25 (2016) 1974–1985. [doi:10.1007/s11665-016-2041-4](https://doi.org/10.1007/s11665-016-2041-4)
- [17] Q. S. Yang, B. Jiang, Q. Xiang, S. Q. Luo, X. W. Yu, F. S. Pan, Microstructure evolution and corrosion performance of AZ31 magnesium alloy sheets, *Rare Metal Materials and Engineering* 45 (2016) 1674–1677.

- [18] J. J. He, B. Jiang, J. Xu, J. Y. Zhang, X. W. Yu, B. Liu, F. S. Pan, Effect of texture symmetry on mechanical performance and corrosion resistance of magnesium alloy sheet, *Journal of Alloys & Compounds* 723 (2017) 213–224. [doi:10.1016/J.JALLCOM.2017.06.269](https://doi.org/10.1016/J.JALLCOM.2017.06.269)
- [19] G. Song, R. Mishra, Z. Xu, Crystallographic orientation and electrochemical activity of AZ31 Mg alloy, *Electrochemistry Communications* 12 (2010) 1009–1012. [doi:10.1016/j.elecom.2010.05.011](https://doi.org/10.1016/j.elecom.2010.05.011)
- [20] Y. Luo, Y. Deng, L. Guan, L. Ye, X. Guo, A. Luo, Effect of grain size and crystal orientation on the corrosion behavior of as-extruded Mg-6Gd-2Y-0.2Zr alloy, *Corrosion Science* 164 (2020) 108338. [doi:10.1016/j.corsci.2019.108338](https://doi.org/10.1016/j.corsci.2019.108338)
- [21] Y. H. Bao, L. Chen, J. W. Tang, Z. G. Li, G. Q. Zhao, C. S. Zhang, Investigation on corrosion behavior and mechanical properties of an extruded Mg-Zn-Al-Sn-Mn alloy, *Materials Characterization* 180 (2021) 111439. [doi:10.1016/j.matchar.2021.111439](https://doi.org/10.1016/j.matchar.2021.111439)
- [22] M. Ben-Haroush, G. Ben-Hamu, D. Eliezer, L. Wagner, The relation between microstructure and corrosion behavior of AZ80 Mg alloy following different extrusion temperatures, *Corrosion Science* 50 (2008) 1766–1778. [doi:10.1016/j.corsci.2008.03.003](https://doi.org/10.1016/j.corsci.2008.03.003)
- [23] S. A. Zhang, B. C. Liu, M. X. Li, H. Y. Wang, Y. L. Ma, Effect of microstructures and textures on different surfaces on corrosion behavior of an as-extruded ATZ411 magnesium alloy sheet, *Acta Metallurgica Sinica – English Letters* 34 (2021) 1029–1041. [doi:10.1007/s40195-021-01203-7](https://doi.org/10.1007/s40195-021-01203-7)
- [24] Y. Wang, F. Li, X. W. Li, W. B. Fang, Unusual texture formation and mechanical property in AZ31 magnesium alloy sheets processed by CVCDE, *Journal of Materials Processing Technology* 275 (2020) 116360. [doi:10.1016/J.JMATPROTEC.2019.116360](https://doi.org/10.1016/J.JMATPROTEC.2019.116360)
- [25] S. M. Fatemi, A. Zarei-Hanzaki, M. Eskandari, M. Haghshenas, Alleviation of mechanical anisotropy in ultrafine/nano-grained AZ31 magnesium alloy, *Journal of Materials Engineering and Performance* 27 (2018) 4270–4279. [doi:10.1007/s11665-018-3485-5](https://doi.org/10.1007/s11665-018-3485-5)
- [26] T. Mayama, M. Noda, R. Chiba, M. Kuroda, Crystal plasticity analysis of texture development in magnesium alloy during extrusion, *International Journal of Plasticity* 27 (2011) 1916–1935. [doi:10.1016/j.ijplas.2011.02.007](https://doi.org/10.1016/j.ijplas.2011.02.007)
- [27] K. Shiraishi, T. Mayama, M. Yamasaki, Y. Kawamura, Enhanced non-linearity during unloading by LPSO phase in as-cast Mg-Zn-Y alloys and slip-dominated non-linear unloading mechanism, *Materials Science and Engineering A* 790 (2020) 139679. [doi:10.1016/j.msea.2020.139679](https://doi.org/10.1016/j.msea.2020.139679)
- [28] M. Yamasaki, T. Mayama, T. Matsumoto, K. Hagihara, D. Drozdenko, Y. Kawamura, Formation of <0001>-rotation-type kink boundary in Mg-Zn-Y alloy with long-period stacking ordered structure, *Materials Science and Engineering A* 819 (2021) 141466. [doi:10.1016/j.msea.2021.141466](https://doi.org/10.1016/j.msea.2021.141466)
- [29] K. Hagihara, M. Okubo, M. Yamasaki, T. Nakano, Crystal-orientation-dependent corrosion behaviour of single crystals of a pure Mg and Mg-Al and Mg-Cu solid solutions, *Corrosion Science* 109 (2016) 68–85. [doi:10.1016/j.corsci.2016.03.019](https://doi.org/10.1016/j.corsci.2016.03.019)
- [30] G. L. Song, R. Mishra, Z. Xu, Crystallographic orientation and electrochemical activity of AZ31 Mg alloy, *Electrochemistry Communications* 12 (2010) 1009–1012. [doi:10.1016/j.elecom.2010.05.011](https://doi.org/10.1016/j.elecom.2010.05.011)
- [31] Y. L. Huang, H. Shih, H. C. Huang, S. Wu, S. Ramanathan, C. Chang, F. Mansfeld, Evaluation of the corrosion resistance of anodized aluminum 6061 using electrochemical impedance spectroscopy (EIS), *Corros. Sci.* 50 (2008) 3569–3575. [doi:10.1016/j.corsci.2008.09.008](https://doi.org/10.1016/j.corsci.2008.09.008)
- [32] Y. L. Huang, H. Shih, J. Daugherty, F. Mansfeld, Evaluation of the properties of anodized aluminum 6061 subjected to thermal cycling treatment using electrochemical impedance spectroscopy (EIS), *Corros. Sci.* 51 (2009) 2493–2501. [doi:10.1016/j.corsci.2009.06.031](https://doi.org/10.1016/j.corsci.2009.06.031)
- [33] M. Kouhi, A. Mohebbi, M. Mirzaei, Evaluation of the corrosion inhibition effect of micro/nanocapsulated polymeric coatings: A comparative study by use of EIS and Tafel experiments and the area under the Bode plot, *Research on Chemical Intermediates* 39 (2013) 2049–2062. [doi:10.1007/s11164-012-0736-1](https://doi.org/10.1007/s11164-012-0736-1)
- [34] C. R. McCall, M. A. Hill, R. S. Lillard, Crystallographic pitting in magnesium single crystals, *British Corrosion Journal* 40 (2013) 337–343. [doi:10.1179/174327805X66326](https://doi.org/10.1179/174327805X66326)
- [35] G. Han, J. Y. Lee, Y. C. Kim, J. H. Park, D. I. Kim, H. S. Han, S. J. Yang, H. K. Seok, Preferred crystallographic pitting corrosion of pure magnesium in Hanks' solution, *Corrosion Science* 63 (2012) 316–322. [doi:10.1016%2Fj.corsci.2012.06.011](https://doi.org/10.1016%2Fj.corsci.2012.06.011)